

# Ignition detection with the breakdown voltage measurement during nanosecond repetitively pulsed discharges

M. Balmelli<sup>a,b,\*</sup>, L. Merotto<sup>a</sup>, P. Soltic<sup>a</sup>, J. Biela<sup>b</sup>

<sup>a</sup> Empa, Swiss Federal Laboratories for Materials Science and Technology, Überlandstrasse 129, 8600 Dübendorf, Switzerland

<sup>b</sup> Laboratory for High Power Electronic Systems, ETH Zürich, Physikstrasse 3, 8092 Zurich, Switzerland

## ARTICLE INFO

### Keywords:

Nanosecond Repetitively Pulsed Discharge  
ignition (NRPD)  
Ignition detection  
Plasma-assisted ignition  
Ignition  
Flame kernel  
Nanosecond pulse generator

## ABSTRACT

Nanosecond Repetitively Pulsed Discharge (NRPD) is a promising ignition concept for introducing diesel-like process parameters for hard-to-ignite renewable fuels in Spark Ignition (SI) engines. Knowing whether an ignition event initiated by a series of nanosecond electrical discharges was successful or not gives the possibility of using this information for closed-loop ignition control. This paper presents a methodology for detecting successful ignition under NRPD ignition.

After a nanosecond discharge, the heat loss from the particles (plasma-gas) between the electrodes and the surrounding gas is different if a robust flame kernel is established. If a flame kernel is present, the heat losses are lower, resulting in a lower local density of the gas between the electrodes. The breakdown voltage value of a nanosecond pulse is proportional to the local density. A control pulse is applied after the main ignition sequence to detect successful ignition. Lower breakdown voltages of the control pulse are present if a robust early flame kernel is present. The control pulse is applied before the pressure rises due to the presence of fast combustion, allowing ignition to be detected during the inflammation phase, thus allowing the possibility to place additional ignition events, if necessary.

This technique was experimentally analyzed in a Constant Volume ignition Cell (CVC) and in a Rapid Compression Expansion Machine (RCEM). In the CVC at the ignitability limit, lower breakdown voltages of the control pulse are mostly measured when no pressure rise is measured. In the RCEM, the heat release rate is analyzed with a two-zone thermodynamic model, and the early flame kernel formation is monitored with Schlieren imaging. Some overlap exists in the control pulses' breakdown voltages for the ignition and quenching experiments; nevertheless, the Schlieren videos outline that the overlapping cases have a similar flame kernel formation, and the difference arises thereafter.

## 1. Introduction

Robustly igniting air-fuel mixtures is a very important requirement in many applications. Examples are Spark Ignited internal combustion Engines (SI-Engines) and starting combustors for heating purposes or in gas turbine systems.

Introducing hard-to-ignite fuels such as methane, biogas, or sewage gas and modifying the combustion process in SI-Engines to reach diesel-like efficiency (combustion of diluted mixtures or introducing diffusion-controlled spark ignited combustion schemes at high compression ratios) demands novel strategies for robust ignition. In SI-Engines, ignition influences the later stage of combustion. Ignition and early flame development limit the maximal Air-to-Fuel Ratio (AFR) and influence

cycle-to-cycle variation [1]. Classical automotive ignition systems reach their limits for the heavy-duty, off-road, and power generation sectors [2,3]. As an alternative, Nanosecond Repetitively Pulsed Discharge (NRPD) can effectively ignite hard-to-ignite fuel-air mixtures [4–6]. An investigation in an optical pre-chamber has shown that NRPD is advantageous for stable combustion near the ignitability limits compared to a state-of-the-art inductive ignition system [7,8]. Similar findings are reported in [5], where NRPD can better support the initial flame kernel and improve the ignition probability. The initial combustion process inside an optical single-cylinder engine is shortened when nanosecond pulsed ignition is used instead of a conventional ignition system; with shorter pulses, this effect is enhanced [9]. Nitrogen oxide emissions and specific fuel consumption can be reduced in engines when classical

\* Corresponding author at: Empa, Swiss Federal Laboratories for Materials Science and Technology, Überlandstrasse 129, 8600 Dübendorf, Switzerland.

E-mail address: [michelangelo.balmelli@empa.ch](mailto:michelangelo.balmelli@empa.ch) (M. Balmelli).

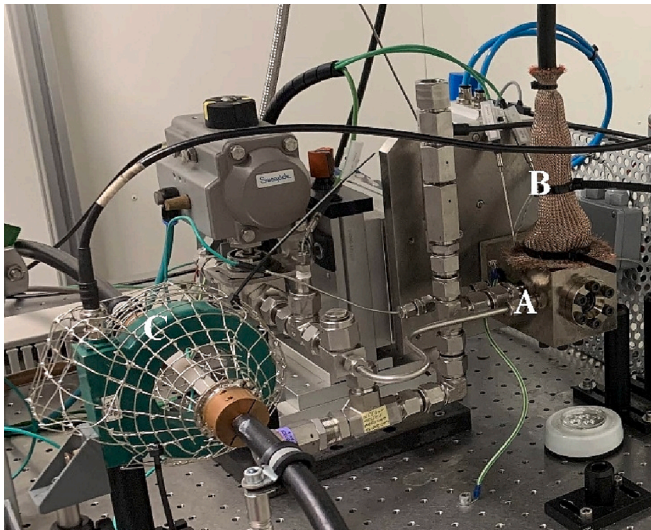


Fig. 1. CVC setup: A-ignition cell, B-coaxial cable shield, C-current shunt.

ignition systems are changed in favor of ignition sources capable of producing NRPD [10,11]. NRPD has also been effectively applied to stabilize the flame in conditions similar to those of second-stage combustors of turbines [12,13].

In SI-Engines, classical inductive or capacitive ignition systems deliver one ignition event per engine cycle; the only actuating variable is the timing of the ignition. If the ignition is unsuccessful or the combustion process is non-optimal, the only possible adjustment is within the following engine cycle, where the fuel quantity or the ignition timing could be adjusted. In contrast, ignition detection during the early stage of combustion, in conjunction with a fast actuator, allows the engine to react to misfires within the same engine cycle. If the detection and actuation are sufficiently rapid, the slight advance of combustion phasing from the ideal location will have a minor impact. With an NRPD system, the number of pulses and the repetition frequency could be varied to stabilize the ignition process. This possibility of reacting on ignition detection is even more interesting for systems with direct fuel injection to the combustion chamber, where additional fuel could be applied within the same engine cycle.

Current measurement by applying a DC voltage after ignition over the sparkplug electrodes in SI-Engines has been successfully used to detect abnormal combustion (misfire and knock) and the location of the peak pressures [14,15]. Several reactions in the combustion process include ions, which are detected by the current measurement and can be used for feedback control. Nevertheless, during early flame kernel formation, ions produced by the electrical discharge are likely still present between the electrodes making the reading inaccurate. Therefore, this technique is best suited for information between cycles, not during the ignition or early flame kernel event itself.

The discharge current and voltage are affected by the surrounding gases. For example, in [16], the authors have shown that the spark discharge duration correlates with the fluid velocity around the sparkplug. Knowing the fluid velocity could help to gain information about the stochastic nature of the turbulence during the ignition event, which is known to impact the cycle-to-cycle variation [17]. Although the flow velocity could affect the later combustion stage and, in extreme cases, also result in flame quenching, knowing the fluid motion around the sparkplug does not directly correlate to reliable ignition detection.

A fast flame detection technique based on the breakdown voltage measurement is introduced in [18], which presented an analysis of a second sparkplug used as a detecting probe. The authors could detect the flame front by applying a voltage slightly below the breakdown threshold across the gap, and once the flame arrives at the probe, the breakdown strength between the gap is reduced, triggering the

breakdown event. The proposed active plasma probing method is much faster than ion current monitoring. It takes only  $10\ \mu\text{s}$  for the voltage to collapse, while it takes  $800\ \mu\text{s}$  for the ion current to rise to the maximal value. This investigation outlines the dependency of the breakdown voltage on the gas composition variation during combustion. However, due to the distance between the two sparkplugs (also physically constrained), this approach is not suited to detect the establishment of the early flame kernel.

The goal of ignition is to start a self-sustained chemical reaction. The plasma expansion following a nanosecond discharge depends on the voltage supply but is not dependent on the mixture composition. Regardless of the plasma condition, there is always a zone where the ideal temperatures for the chemical reaction are present, leading to the establishment of an early flame kernel strongly affected by the gas composition [1,19,20]. The breakdown voltage under NRPD is investigated in [21,22], where it is shown that the peak voltage during a nanosecond discharge depends on the used electrode material and spacing, the density between the electrodes, and the pulse rise rate. After the discharge, the plasma recombination and cooling depend on the heat losses to the electrodes and the surrounding gas temperature. Therefore, it can be expected that if the delay between nanosecond pulses is long enough (on the order of milliseconds), the local density between the electrodes will be affected by the presence and strength of the early flame kernel. This could allow ignition detection by measuring the pulse breakdown voltage after early flame kernel formation, before any pressure increase due to combustion, and before significant flame front expansion. Such a methodology could allow for closed-loop ignition control with NRPD. In addition, detecting the early flame kernel could be valuable for other applications, such as energy-efficient flame stabilization or feedback control of thermoacoustic instabilities in second-stage combustors of gas turbines [23].

A consistent initialization of non-equilibrium plasma discharges for use in engine CFD codes is proposed in [24], where it is shown that the approach produces results that agree with experiments on the ignition of stoichiometric air-methane mixtures. Longer dwell times between pulses require more energy to establish flame propagation. Simulations show that using two  $1.4\ \text{mJ}$  pulses with a  $300\ \mu\text{s}$  dwell time is insufficient to establish a robust flame propagation, and  $300\ \mu\text{s}$  after the second discharge, the temperature between the electrodes falls below  $800\ \text{K}$ . In contrast, when the pulses have a dwell time of  $100\ \mu\text{s}$ , flame propagation is possible. The temperature between the electrodes after  $300\ \mu\text{s}$  exceed  $1500\ \text{K}$ . Due to the minor heat release, the pressure is similar for the two cases, so the local density would be nearly half for the second case. Applying a third nanosecond pulse after  $300\ \mu\text{s}$  would result in different breakdown voltages for the two conditions and, therefore, detect the case where a flame front is present.

This article presents a technique to detect successful ignition for methane-air mixtures ignited by NRPD based on breakdown voltage measurements. The paper is organized as follows: Sections 2.1 and 2.2 present the two experimental setups used. The electrical characterization of NRPD is presented in Section 2.3, focusing on the factors affecting the current-voltage variation during the nanosecond discharge. Sections 2.4 and 2.5 present two methods used to analyze the combustion process. The remaining part of Section 2 is dedicated to the theory needed to understand and motivate the ignition detection technique. Section 3 presents, in the beginning, the analysis of the discharge variation during multiple pulses at high frequency; afterward, the ignition detection investigation results are shown (Sections 3.2 and 3.3). The presented results are then discussed and summarized in Sections 4 and 5.

## 2. Materials and methods

### 2.1. Experimental setup 1: Constant Volume ignition Cell (CVC)

The CVC with a volume of  $20\ \text{cm}^3$  introduced in [25] is used to investigate the ignition of methane-air mixtures with NRPD. A

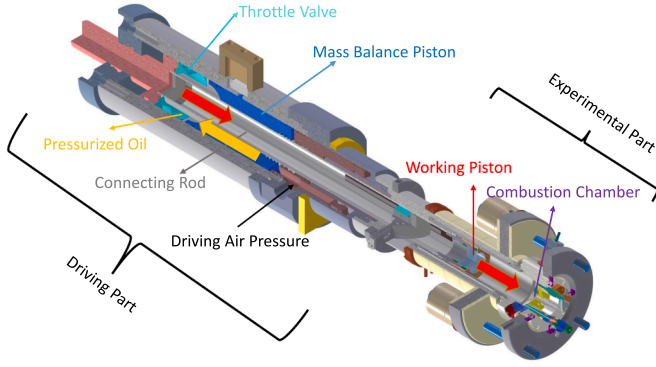


Fig. 2. Schematic of the RCEM, component names, and working principle.

Table 1  
RCEM setup.

Bore	84 mm
Stroke	180 mm
Cylinder head	Flat, two valves
Piston bowl	$d = 52$ mm, 4 mm depth
Side windows' optical access	$d = 36$ mm
In-cylinder pressure measurement 1	Piezoelectric Kistler 7061B ( $\pm 0.5$ %, 0–250 bar)
In-cylinder pressure measurement 2 (used for pressure level correction)	Kistler 4075A10 ( $\pm 1$ %, 0–10 bar), inserted in a fast switching adapter, Kistler 741A
Heating	Cylinder head and liner
Fuel injection system	Skynam DMS06 driver, Bosch HDEV 1 injector
Spark plug	NGK 5096
Ignition system	NRPD, FID 15-10NK
High-speed camera	LaVision HSS6
Light source (Xenon)	Anklin Xenon Nova 300
Plano-convex lens	PCX 75 $\times$ 250 vis 0 (Diameter $\times$ focal distance mm)

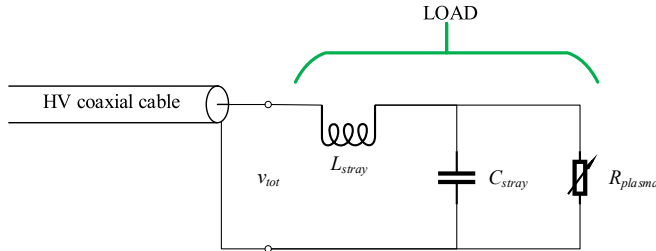


Fig. 3. Equivalent electrical circuit of the sparkplug.

commercial pulse generator from FID GmbH (model FID 15-10NK) generates nanosecond pulses of 50 ns duration and up to a 10 kHz Pulse Repetition Frequency (PRF). The maximal pulse amplitude over a 100  $\Omega$  load is 15 kV. The pulse rise rate is 3–5 ns from 10 % to 50 % of the maximum. The Berkley Nucleonics 577 delay generator precisely controls each pulse delivered to the pulse generator. The pulse generator is connected via a 30 m coaxial cable with an impedance ( $Z$ ) of 75  $\Omega$  to non-resistive sparkplugs. The voltage and current at the sparkplug are reconstructed with a shunt measurement in the middle of the 30 m cable using a Pearson current monitor (model 6584). The coaxial cable's core is connected to the high-voltage sparkplug's electrode, while the coaxial cable's shield is connected to the ground electrode through the ignition cell. Fig. 1 shows a picture of the CVC setup.

Two sparkplugs are used in the present work: a J-gap sparkplug (NGK 5096) and a surface gap sparkplug (NGK 2522); appendix b provides pictures of the sparkplugs. The setup and current measurement technique are described and validated in [21,22]. The error in the voltage

measurement depends on the current probe with a precision of 1 % and a sensitivity of 1 V/A, which is attenuated four times to display on an oscilloscope with a DC gain accuracy of full scale (40 V) of 1.5 %. Assuming the worst-case scenario of linear error propagation, the error on a typically measured breakdown voltage of 10 kV is 5 %. Bronkhorst mass flow controllers allow for the precise adjustment of the methane-air equivalence ratio. In addition, the cell filling pressure is adjusted by an absolute pressure sensor (Keller PAA-33X with a precision of  $\pm 20$  mbar), while the combustion is monitored by a piezoelectric pressure transducer (Kistler 6052C with an accuracy of  $\pm 0.5$  %) [26].

## 2.2. Experimental setup 2: Rapid Compression Expansion Machine (RCEM)

The Rapid Compression Expansion Machine (RCEM) is a free-floating piston test rig with optical access through the cylinder head. Its advantage is that thermodynamic conditions can be reproduced, such as those in internal combustion engines or the second stages of turbine combustors. The RCEM has been successfully used for single-cycle investigations of hydrogen-air and hydrogen-enriched methane-air mixture combustion [20,27], pre-chamber ignition [28], diesel-pilot ignited methane mixtures [29], and Homogenous Charge Compression Ignition (HCCI) combustion [30]. The RCEM has been extensively modified over the years to allow for different investigations. The working principle and the specification in the current configuration are detailed below. The machine consists of two main sections, the driving and experimental parts, connected by a rod. Fig. 2 depicts a schematic of the RCEM where the names of the components are reported. The red arrows represent the motion of the pistons during fast compression.

A mass balance piston that allows for nearly vibration-free operations divides the two parts and moves in the opposite direction of the working piston. After the combustion chamber's scavenging procedure, the experiment starts by pushing the piston to Bottom Dead Center (BDC) and setting the driving air pressure to the desired value. Afterward, the combustion chamber is filled with air at 1.2 bar. The connecting rod at the BDC is inside a sealed cavity that prevents the pressurized oil from acting on the connecting rod (starting position). The compression stroke begins by opening a valve that connects the pressurized oil to the back of the piston rod and slowly pushes the piston out of the starting position. During this slow, throttled motion, fuel is injected into the combustion chamber. Due to the high injection pressures used ( $\sim 100$  bar) and the long time before the rapid compression starts ( $\sim 2$  s), the fuel has enough time and momentum to mix perfectly. The feed pressure is regulated with pressure regulators, and the injector's voltage profile is controlled with a Skynam DMS06 driver. When the connecting rod exits the throttle valve, the pneumatic force of the air is transmitted to the oil via the mass balance piston that now acts on the full area of the rod. The pressure difference between the driving volume and the combustion chamber now determines the acceleration of the moving parts. The compression increases the pressure inside the combustion chamber, slowing the piston. The combustion further increases the pressure in the combustion chamber, pushing the piston back. The movement of the piston is determined by the kinetics of the process and not by kinematics, as is the case with conventional reciprocating engines. For the RCEM experiments, only the J gap sparkplug is used with the same ignition systems as in the CVC. Table 1 lists the RCEM specifications.

## 2.3. Electrical characterization

The pulse propagation time in the coaxial cable depends on the cable's capacitance and inductance per unit length. For the used cable, the propagation time is ca. five nanoseconds per meter [31]. Therefore, the 50 ns long pulse is entirely contained inside ten meters of cable. The resulting setup can be described as a transmission line circuit [32]. A reflection occurs if the load impedance does not coincide with the



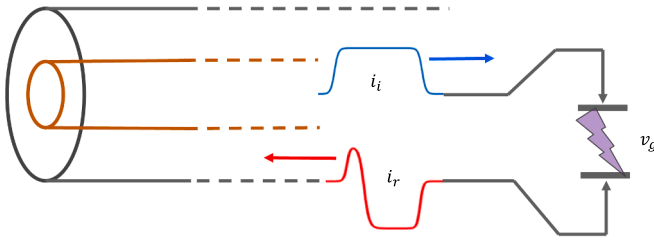


Fig. 4. Discharge scheme.

Table 2

Regimes occurring during a nanoseconds pulsed discharge.

	Air/plasma resistance	Voltage reflected	Gap voltage	Gap current	Input power
Low current discharge (open-load)	$R \gg Z$	$v_r = v_i$	$v_g = 2v_i$	$i_g = 0$	$p_g = 0$
Matching impedance (matched-load)	$R = Z$	$v_r = 0$	$v_g = v_i$	$i_g = \frac{v_i}{Z}$	$p_g = \frac{v_i^2}{Z}$
High current discharge (short-load)	$R \ll Z$	$v_r = -v_i$	$v_g = 0$	$i_g = \frac{2v_i}{Z}$	$p_g = 0$

cable's impedance ( $Z$ ). The total voltage ( $v_{tot}$ ) and current ( $i_{tot}$ ) at the load are described by Equation (1) and Equation (2), where indices “ $i$ ” and “ $r$ ” are used for the incident and reflected waves, respectively.

$$v_{tot} = v_i + v_r \quad (1)$$

$$i_{tot} = i_i - i_r \quad (2)$$

The equivalent circuit for a coaxial cable connected to a sparkplug is depicted in Fig. 3. The load (sparkplug) is composed of a stray capacitance, a stray inductance, and a time-varying resistance. Because the load is compact (propagation time  $< 1$  ns), the load can be treated as lumped.

Due to the fast voltages and current transients, even small capacitance ( $C_{stray}$ ) and inductance ( $L_{stray}$ ) typical of sparkplugs (5–15 pF and 5–10 nH [1,22,33]) could affect the current and voltage variation. With the used pulse generator (rise time  $\sim 10$  ns), the stray parameters have a negligible impact on the voltage measurement over the spark gap before breakdown. The comparably small displacement currents ( $\sim 20$  A) during the voltage increase are insufficient to generate an appreciable voltage over the stray inductance. During the discharge, the currents and voltages vary faster than during the voltage rise and should be considered for the precise calculation of the electric field applied to the plasma and its electrical resistance.

Because the breakdown voltage value and the qualitative analysis of the discharge are not affected by the stray parameters, the stray inductance and capacitance are neglected in this work. Therefore, the load is purely resistive ( $R$ ) and depends solely on the plasma conductance. Notably, the total energy deposition, total current, and voltage measurements are not affected by the assumption of a purely resistive load. This assumption is helpful for the comprehension of the results. Therefore the termination is hereafter referred to as plasma resistance.

When a pulse (voltage  $v_i$ , current  $i_i$ ) arrives at the sparkplug, it is in part reflected and in part transmitted depending on the ratio between the varying air-plasma electrical resistance ( $R$ ) and the coaxial cable impedance ( $Z$ ). Before breakdown, air offers high resistance, and the pulse is reflected with the same polarity as the incident pulse. After breakdown, the electron density rapidly increases and reduces the electrical resistance to low values. When the plasma resistance is small (compared to the cable impedance), high currents flow through the gap, and the polarity of the reflection is inverted to the incident pulse

polarity resulting in a low voltage drop over the gap. Fig. 4 shows a schematic representation of the discharge; the blue and red waveforms are used for the incident and reflected currents, respectively.

The cable impedance links the current and voltage inside a coaxial cable. Therefore, the incident and reflected pulse current waveform measurements allow for calculating the voltage and current, according to Equation (3) and Equation (4), respectively.

$$v_g = Z(i_i + i_r) = Zi_i \frac{2R}{Z + R} \quad (3)$$

$$i_g = i_i - i_r = i_i \frac{2Z}{Z + R} \quad (4)$$

When the nanosecond pulse amplitude is high enough, there is a transition from streamer to spark [4]. During the spark phase, the current rises to several hundred amperes. Therefore, the electrical resistance between the electrodes varies by several orders of magnitude. Before the breakdown, the air-gas mixture acts as a good insulator. The resistance between the electrodes can be assumed to have an infinite resistance when compared to the coaxial cable impedance. The generated transient plasma with high electron density is a good conductor. The 75  $\Omega$  cable impedance is negligible compared to the air-gas resistance ( $Z \ll R$ ), whereas it is the only factor to consider when a spark is present ( $Z \gg R$ ). Two extreme regimes are recognizable from Equation (3) and Equation (4): a doubling of the pulse voltage when air is between the electrodes (low current discharge), and a limitation of the transmitted current when the electron density is high (high current discharge). An intermediate regime (matching impedance) can be recognized where the power to the plasma is the highest, no reflection occurs, the total power is absorbed from the gas, and the plasma resistance is equal to the cable impedance. The features of these three regimes are summarized in Table 2.

The cumulative energy per pulse deposited to the plasma (plasma energy) is calculated according to Equation (5).

$$E_{plasma} = \int_{t_0}^{t_{end}} p_g(t) dt = \int_{t_0}^{t_{end}} i_g(t) v_g(t) dt \quad (5)$$

The efficiency of the NRPD discharge is defined as the ratio of the plasma to the pulse energy, according to Equation (6). The pulse energy is the energy that would be deposited to an ideal load with resistance equal to the cable impedance (matched-load). The efficiency is zero for low-current (open-load) and high-current (short-load) cases.

$$\eta = \frac{E_{plasma}}{\int_{t_0}^{t_{end}} \frac{v_i^2}{Z} dt} \quad (6)$$

During a nanosecond discharge, the air plasma resistance undergoes the three regimes; therefore, its efficiency is always below unity. Higher efficiencies are reached the longer the plasma resistance is close to the cable impedance. The detailed measurement technique and factors that affect the breakdown voltage are described in [22].

#### 2.4. Heat release rate analysis

The combustion Heat Release Rate (HRR) inside the RCEM is estimated using a 2-zone thermodynamic model, accounting for compression and expansion heating, wall heat losses, crevice volumes, and blow-by [34].

The calculation uses the working piston position and the measured cylinder pressure value. The data from both pressure sensors, the piezoelectric as well as the piezoresistive, are acquired at a 100 kHz sampling rate. The pressure trace is derived from the piezoelectric sensor pegged during the compression stroke using the piezoresistive sensor. The piston position is acquired with a 100 kHz sampling rate, and the sensor has a 0.02 mm resolution with an error below 0.1 %.



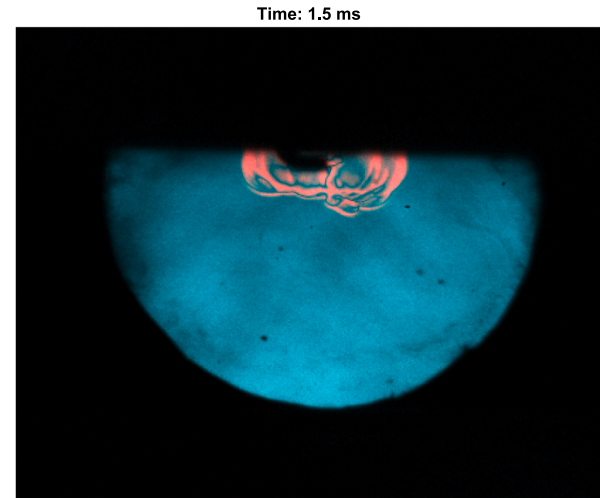
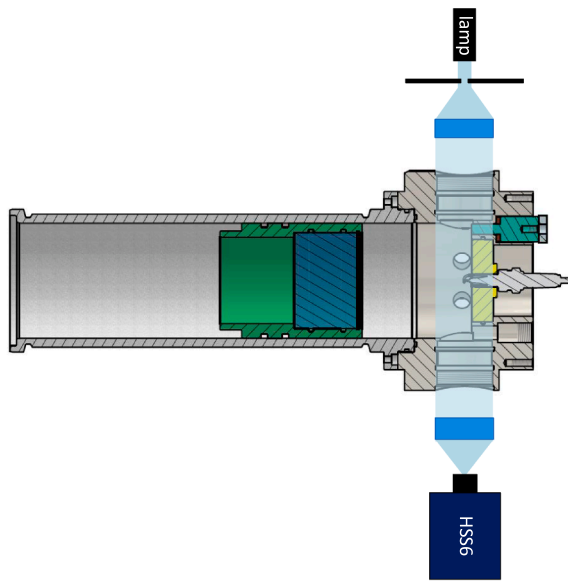


Fig. 5. Left, Schlieren setup in the RCEM through the cylinder head. Right, post processed high-speed frame.

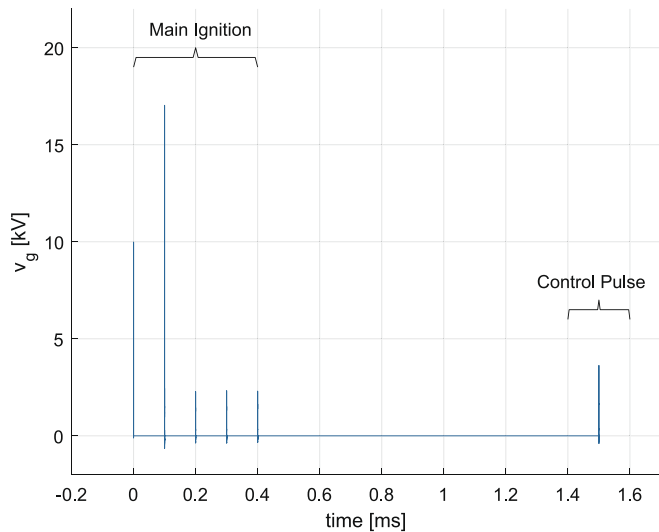


Fig. 6. Pulse pattern used for ignition detection in the RCEM.

## 2.5. Schlieren imaging

Fig. 5 (left) shows the Schlieren setup in the RCEM. A xenon lamp is used with a diaphragm to focus the light into a plano-convex lens to create collimated light. The collimated light enters the combustion chamber through the side window. Collimated light exits on the opposite window and is refocused through a plano-convex lens into an HSSX high-speed camera.

The diaphragm is placed at the focal point of the convex lens to eliminate diverging beams and increase the sensitivity gradients of the setup. The video is recorded with a  $672 \times 1024$  pixel resolution at 20,000 FPS and an exposure of  $2.5 \mu\text{s}$ .

For analysis and better visualization, the videos are post processed. After ignition, each frame is compared against a background image to detect the apparent flame front. Suppose the intensity difference in one pixel is above a set threshold; then that pixel is treated as the flame front. Fig. 5 right shows one post processed frame at 1.5 ms after ignition. Blue colors are used to depict what is treated as background, while the red colors mark the apparent flame front.

## 2.6. Ignition detection

The breakdown voltage under slowly increasing voltages scales approximately linearly with the density in the geometry under analysis [22]. The breakdown voltage of nanosecond pulsed discharges depends on the static breakdown voltage and on the pulse rise rate [22]. The scatter of this value depends on the appearance of the seed electron that starts the electron avalanche called the statistical time lag. The statistical time lag exponentially decreases at high electric fields [21]. These two features outline that even though large voltage transients are present under NRPD, the breakdown voltage value is still highly dependent on the local density if the pulse rise rate and electrode spacing are kept constant.

In SI-Engines, combustion is initiated with an electrical discharge. During a nanosecond discharge during the first few tens of nanoseconds, the gas heats to approximately 50,000 K, and the pressure increases. The plasma is fully dissociated and ionized [35]. Following the discharge, a strong shock wave expands the plasma kernel, decreasing the pressure and temperature [1,35]. During the expansion, the plasma recombines, and if the mixture is ignitable, its surface turns into the flame front, a thin reaction sheet where the chemical reactions occur. While the initial plasma kernel growth ( $<100 \mu\text{s}$ ) is not affected by the Air-to-Fuel Ratio (AFR), the following inflammation process is strongly affected by the gas composition, the flame curvature and stretch, and the flow velocity in the vicinity of the sparkplug. Following inflammation, a turbulent flame develops [19].

The idea behind the ignition detection technique is that inflammation affects the local density following the nanosecond pulse after plasma kernel expansion. If the inflammation is successful, the heat losses from the gas present between the electrodes and the surrounding burned gas are lower than if the early flame is quenched. Lower heat losses will result in a lower local density. If a further nanosecond pulse is applied after the plasma kernel expansion, the breakdown voltage provides insight into the local density and, therefore, the inflammation process. Furthermore, different AFRs result in different burned gas temperatures and, therefore, different cooling rates and local densities.

The NRPD ignition pulse pattern for ignition detection purposes is therefore composed of the main pulse sequence at high PRF and an additional (control) pulse after a delay. Fig. 6 shows the voltage at the gap for a representative experiment in the RCEM.

The main ignition sequence is composed of five pulses at 10 kHz, and the control pulse is placed 1.5 ms after the start of ignition.

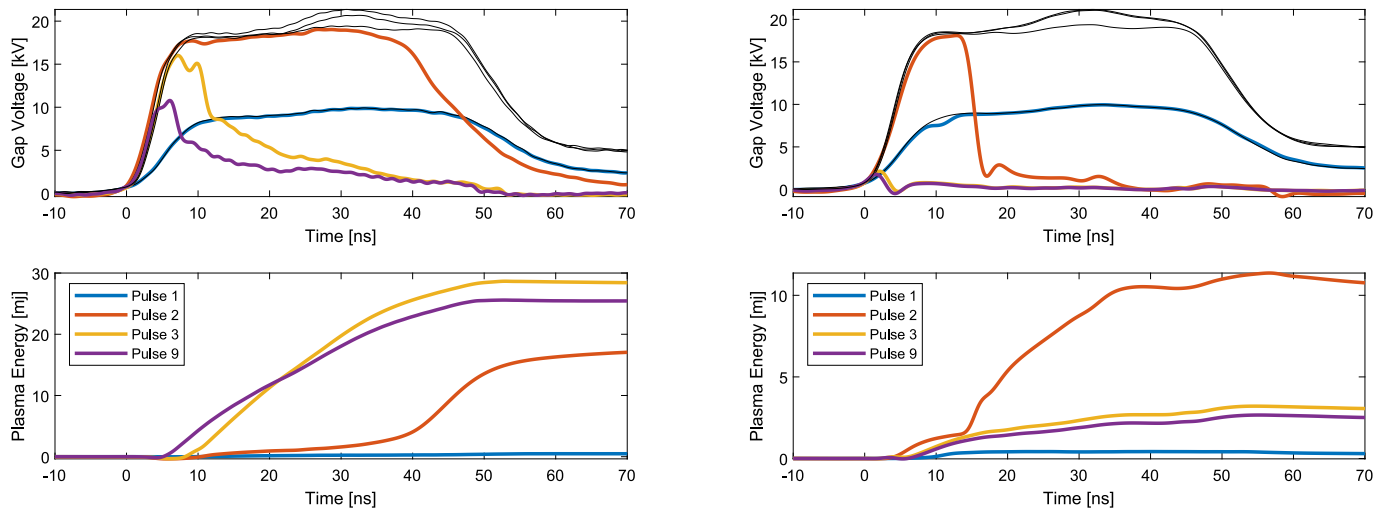


Fig. 7. Pulse voltage waveform for pulses 1, 2, 3, and 9 in a ten-pulse ignition sequence at 10 kHz PRF and 10 bar, on the left for the surface gap sparkplug and on the right for a J-gap sparkplug.

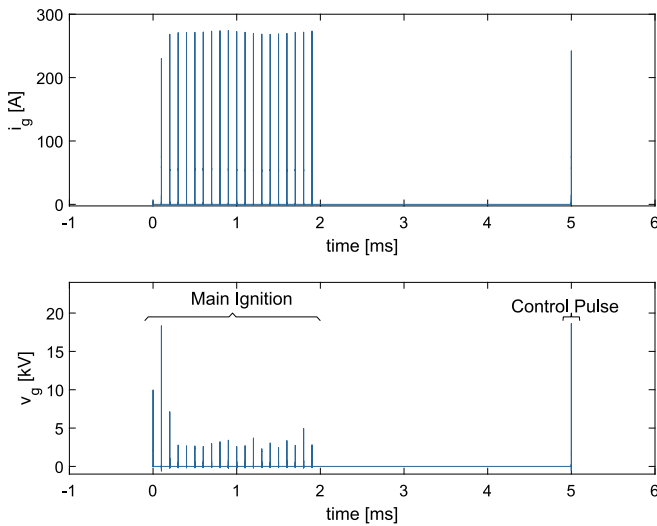


Fig. 8. Pulse pattern for ignition detection, 5 bar  $\lambda = 1.5$ , J-gap sparkplug.

### 3. Results

The results chapter is divided as follows: Section 3.1 outlines the discharge features of the main ignition sequence for the two used sparkplugs performed in the CVC. This investigation is carried out at 10 bar and ambient temperature. Section 3.2 presents the analysis of the ignition detection technique in the CVC performed at the ignitability limit. Moreover, also reported in Section 3.2 is a total of 190 experiments performed at two pressures, with the two sparkplugs and various delays between the main ignition sequence and the control pulse. Finally, Section 3.2 presents the ignition detection investigation performed in the RCEM. Sixty experiments are analyzed with the same pulse pattern at a constant ignition timing for different AFRs.

#### 3.1. Discharge analysis during multiple high voltage nanosecond pulses at 10 kHz PRF

Fig. 7 (upper left and right) shows the evolution of the voltage between the sparkplug electrodes for the two different sparkplugs. Ten pulses at 10 kHz are applied in both experiments at a pressure of 10 bar and ambient temperature. The cell is filled with air and methane with an air-to-fuel ratio of  $\lambda = 1.6$  for the surface gap sparkplug and  $\lambda = 1.35$  for

the J-gap sparkplug.

The start of each pulse is shifted to zero time to match each pulse with the first pulse on a nanosecond timescale. The gap voltage for the first, second, third, and ninth pulses is depicted in the upper subplots in different colors. The maximal voltages that would appear across the gap if no discharge were present are shown in black for the same pulses. The cumulative energy deposited to the plasma, calculated according to Equation (5) is plotted for the same pulses with the same color scheme in the bottom subplots.

The first pulse is of lower amplitude, which frequently occurs due to the internal circuit of the pulse generator. The first breakdown voltages are similar for the two different sparkplugs (ca. 18 kV) and at the second pulse. The time at which breakdown occurs varies between the two experiments and is approximately 15 and 30 ns after the start of the pulse.

Similar energy deposition in the two cases is achieved with the first discharge (pulse 2) and amounts to 15 mJ and 11 mJ, respectively. The energy deposition and maximal gap voltage per pulse decrease rapidly for the J-gap sparkplug. After one pulse, the energy per discharge is approximately constant at ca. 3 mJ. Additionally, for the surface sparkplug, the maximal gap voltage decreases but at a much slower pace. In fact, due to the longer discharge time available (the breakdown happens earlier) and the still relatively high maximal gap voltage of 16 kV, the energy deposit to the plasma increases for the third pulse up to 28 mJ. Afterward, the breakdown voltage decreases, as does the plasma's energy back to ca. 25 mJ.

The energy deposition to the plasma is the highest when the cable impedance links the current and gap voltage, according to Equation (7). When this condition is fulfilled, the plasma impedance equals that of the cable; there is no reflection and, therefore, no energy dissipation.

$$U_{\text{gap}, P_{\text{max}}} = I_{\text{gap}, P_{\text{max}}} Z \quad (7)$$

Assuming that the impedance varies linearly from infinity to zero during the transition from streamer to spark, higher plasma energy is achieved with a lower voltage decrease rate. Slower voltage decrease rates after a breakdown are visible for the surface sparkplug. The efficiency of discharge for the surface gap sparkplug is 39 %, while that for the J-gap sparkplug is approximately 7 %.

#### 3.2. Ignition detection in the constant volume cell

Fig. 8 shows the gap current and voltage for a 20-pulse ignition at 10 kHz with one control pulse 5 ms after ignition start using the J-gap sparkplug.

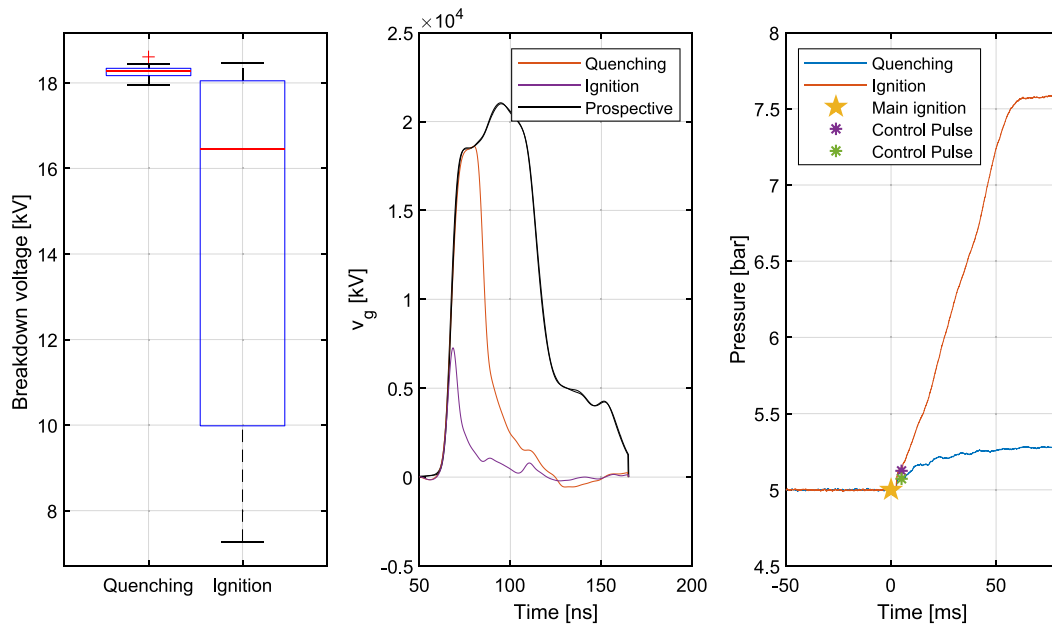


**Fig. 9.** Ignition detection for the J-gap sparkplug, 50 repetitions, 5 bar, and  $\lambda = 1.5$ . Statistics boxplot (left), voltage waveforms (middle) and pressure evolution (right) of the extreme cases.

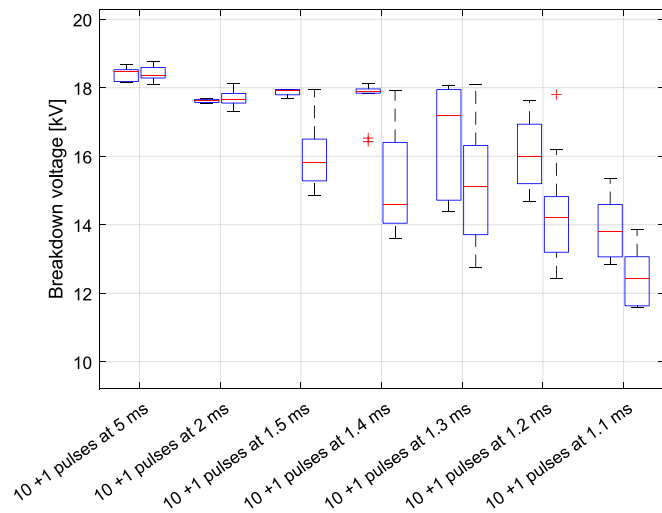


**Fig. 10.** Statistical boxplot of the ignition detection with the surface gap sparkplug for different delays of the control pulse, 20 repetitions each, 10 Bar,  $\lambda = 1.35$ , and surface sparkplug.

The first pulse was not enough to achieve breakdown, visible from the low peak gap current. The measured 5 A peak current for the first pulse is in line with the expected capacitive current for the present voltage rise rate and the capacitance of the sparkplug. The second pulse is the first one where the breakdown is possible due to the higher pulse amplitude at approximately 18 kV. For the following pulses at 10 kHz (0.2–1.9 ms), the maximal voltage between the electrodes is approximately 2.5 kV. The reduced local density between the electrodes due to the heating resulting from the previous pulse and the presence of active and charged species can explain this behavior.

The pulse used to evaluate the ignition is the control pulse at 5 ms. The control pulse's maximal gap voltage for the depicted case is 7.3 kV, and the energy it deposits to the plasma is 13 mJ.

Fig. 9 (left) summarizes the results of 50 repetitions at 5 bar, ambient temperature, and a  $\lambda$  of 1.5 with the same pulse pattern as above, the effectiveness of the ignition detection method. An ignition is treated as

successful if, the pressure increases by more than one bar. On the left, a boxplot is used to group the statistics of the breakdown voltage where ignition was successful and where quenching was present. The red vertical line depicts the median, while the blue rectangle outlines the region between the 25th and 75th percentiles, and the black marks extend to the most extreme data point. The red plus represents the outliers. In the middle, the waveforms of the recorded voltages during the control pulse for the extreme cases of ignition (highest breakdown voltage red line) and quenching (lowest breakdown voltage purple line) are depicted. The black lines on the same plot are used to show the voltage that would develop over the gap if there was no breakdown (prospective voltage). On the right, the pressure against time is also reported for the two extreme cases.

Breakdown voltages above 18 kV were measured for the nine cases where no ignition was detected, while voltages as low as 7.3 kV were measured when the pressure rise suggested successful ignition. The two black waveforms in Fig. 9 left overlap, outlining that the difference in breakdown voltage is not due to different applied voltages. The pressure waveforms against time show that the control pulse is applied before a significant pressure rise due to combustion are present.

Fig. 10 depicts the statistics of the ignition detection for different delay times of the control pulse for the surface sparkplug operated at  $\lambda = 1.35$  and 10 bar. Each group comprises two boxplots, one for the cases where ignition was successful (right), and one for the cases where quenching occurred (left). The main ignition is performed with ten pulses at 10 kHz.

For delay times below 1.5, the statistics indicate the possibility of distinguishing between ignition and quenching. Nevertheless, it is clear that some overlap is present. The control pulse is always placed before a notable pressure increase inside the constant volume cell and is thus feasible for a possible closed-loop reaction scheme.

### 3.3. RCEM experiment

The rapid compression before combustion in the RCEM replicates pressure and temperature conditions at ignition timing much closer to those of an Engine when compared to the CVC setup. The geometry and piston motion allow for flame propagations and HRR similar to those in engines. Furthermore, the optical accesses allow for analyzing the



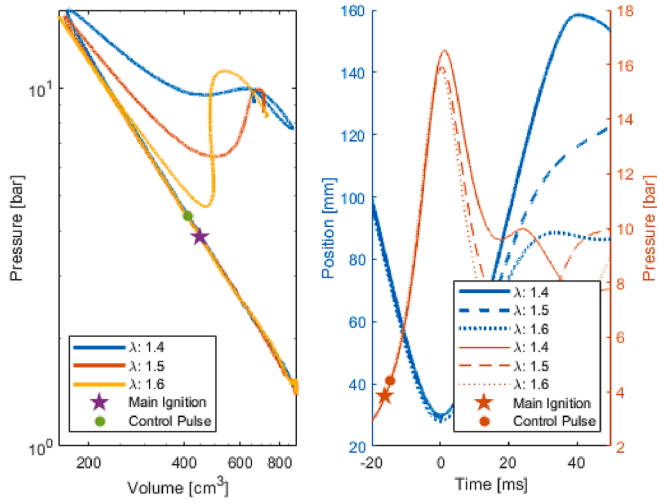


Fig. 11. Pressure traces in the RCEM: pressure, volume (left); pressure and position vs. time (right).

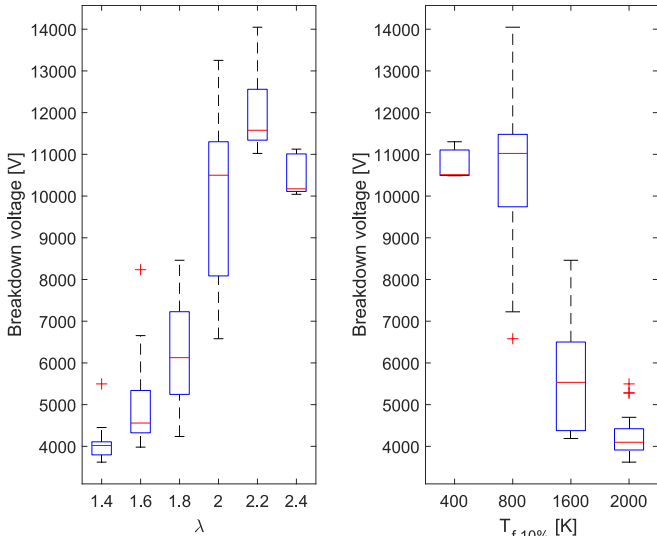


Fig. 12. Boxplots of the control pulse breakdown voltage vs.  $\lambda$  (left) and vs. flame temperature (right).

ignition event and early flame propagation with Schlieren imaging. The RCEM is therefore used to analyze the ignition detection technique by performing six sets of experiments, each with ten repetitions. The same parameters are used in each experiment except for the injected methane mass. This results in the same pressure and temperature trajectory during compression but different expansion trajectories, depending on the combustion. During the filling process, the air mass slightly scatters between different experiments, which results in a slight variation in  $\lambda$  (up to 7 %). The walls of the RCEM are heated to 60 °C, and the compression process further increases the temperature before ignition. For these experiments, the J-gap sparkplug is used. The main ignition is achieved with five pulses at 10 kHz, and the control pulse is at 1.5 ms.

Fig. 11 (left) shows in double logarithmic scale the pressure–volume trace for three different experiments having three different  $\lambda$  values; the star represents the spark timing, while the dots represent the control pulses' location. In Fig. 11 (right), the pressures and piston positions are depicted against time (in red and blue, respectively).

A straight line in the double logarithmic plot shows that the compression process is very close to polytropic, because, for a polytropic change of state,  $pV^m$  is constant (with  $p$  being the pressure,  $V$  the volume,

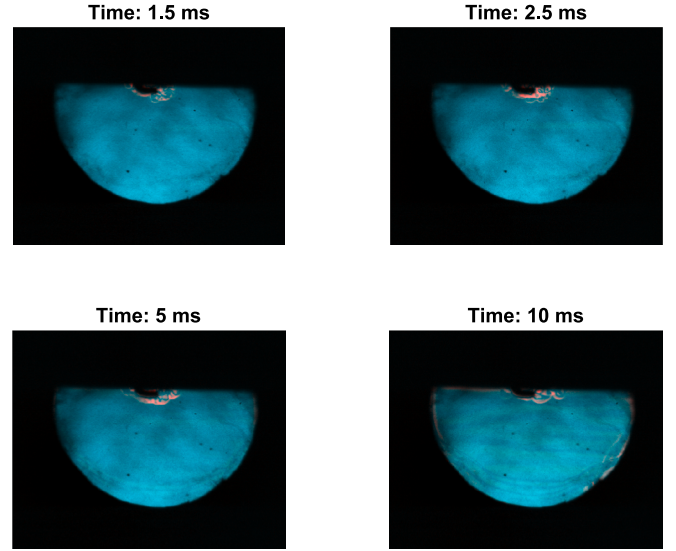


Fig. 13. Four frames of the high-speed Schlieren video for the maximum recorded voltage of the control pulse (breakdown voltage of 14 kV,  $\lambda = 2.2$ ).

and  $n$  the polytropic exponent). The location of the control pulse is well before the deviation from the straight line outlining that the detection of successful ignition is achieved before notable heat release takes place.

From the right subplot, it can be seen that the combustion process influences the piston motion in the RCEM. In fact, a faster pressure increase after Top Dead Center (TDC) results in a higher piston acceleration. During compression, the pressure traces for the different experiments overlap before ignition. After ignition, there is a rather long time when the pressure curves still overlap because the heat release rate is slow. The pressure curves diverge only after the combustion process starts.

The spark timing in SI-Engines is usually adjusted to achieve (whenever possible) the best efficiency. This results in having the center of combustion at a rather constant position, usually at 8 °CA after TDC. Variation in spark timing results in different breakdown voltages due to increasing density during compression. For the current investigation, the spark timing is kept constant to test the ignition detection technique without additional variation and to have similar densities at ignition timing for the different operating points tested.

Fig. 12 shows the statistics of the control pulses' breakdown voltage against  $\lambda$  on the left. Fig. 12 on the right shows the breakdown voltage against the burned gas temperature when 10 % of the fuel mass is burned, estimated with the two-zone thermodynamic model [34].

The median of the control pulses' breakdown voltage increases with increasing  $\lambda$ , except for the last group ( $\lambda = 2.4$ ). The scatter of the data tends to increase as well. The inverse trend is recognized for an increasing temperature of the burned zone.

Fig. 13 shows four images at 1.5, 2.5, 5, and 10 ms taken from the Schlieren recording for the experiments where the highest breakdown voltage of 14 kV was recorded.

In this experiment, it can be seen that the zone that reacts does not show a clear flame front when the control pulse is applied (1.5 ms) and that at 10 ms, hardly any difference in density can be seen from the Schlieren video. This indicates that there was no successful initiation of a combustion process.

Fig. 14 shows four frames where the lowest breakdown voltage of 3.6 kV is recorded.

In this case ( $\lambda = 1.4$ ), a clear flame front can be detected at the end of the ignition process (1.5 ms).

Fig. 15 shows, on the left, the voltage waveforms of the two extreme cases reported in Fig. 13 (blue) and Fig. 14 (red). On the right, the burned and unburned zone temperatures from the HRR analysis are

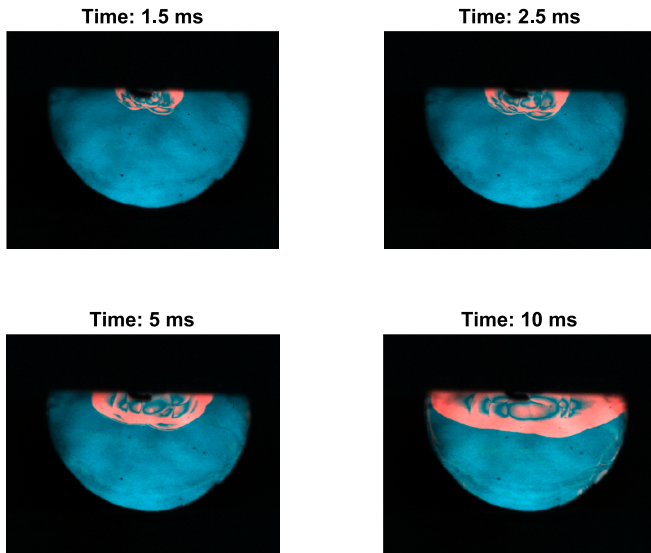


**Fig. 14.** Four frames of the high-speed Schlieren video for the minimum recorded voltage of the control pulse (breakdown voltage of 3.6 kV,  $\lambda = 1.4$ ).

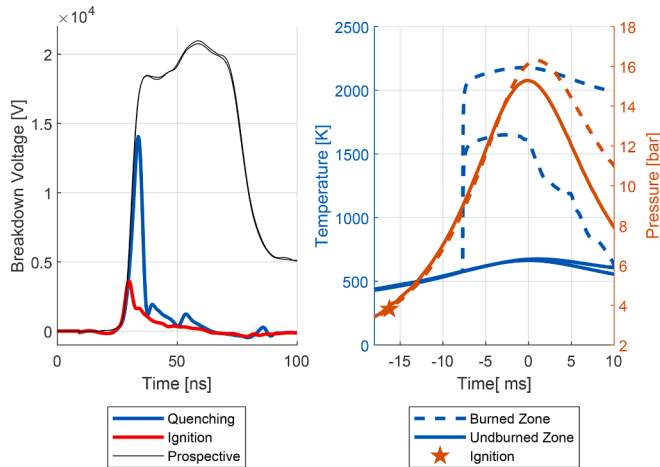


**Fig. 15.** Voltage waveform of the extreme cases (left) and temperature evolution from two-zone thermodynamic analysis (right).

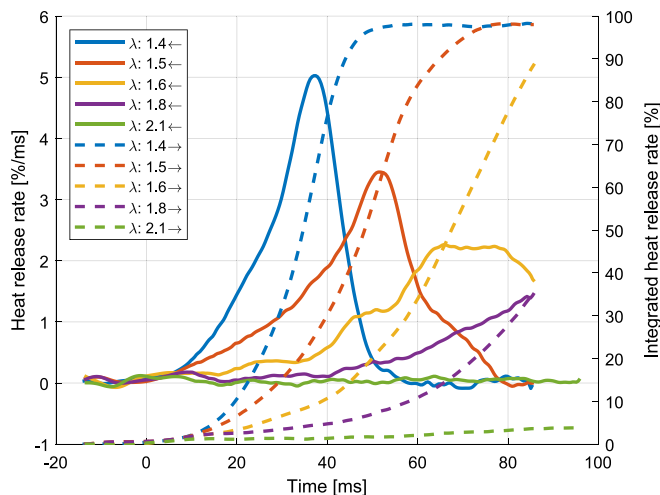


**Fig. 16.** HRR of 5 experiments in the RCEM with varying AFR.

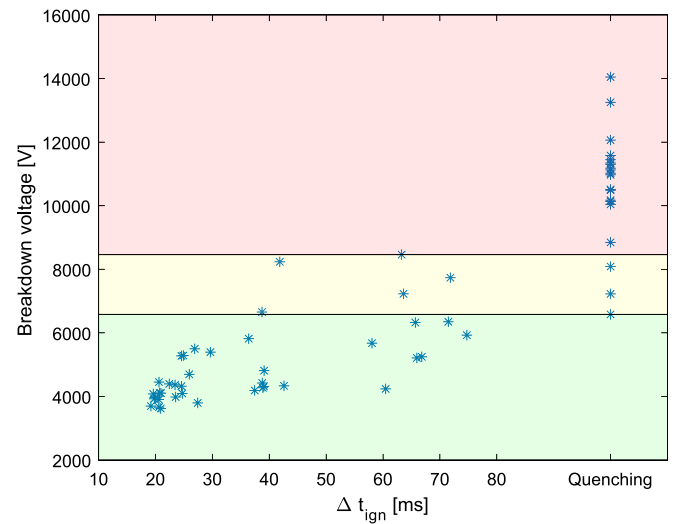


**Fig. 17.** Breakdown voltage of the control pulse vs. ignition delay in the RCEM for all the experiments in the RCEM.

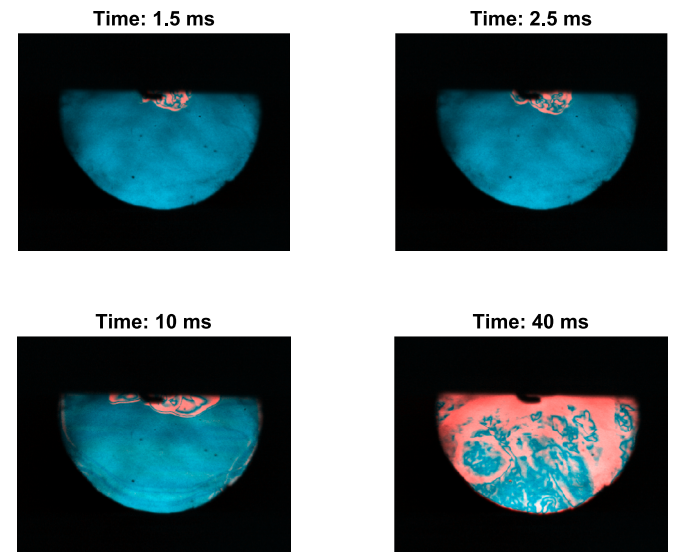


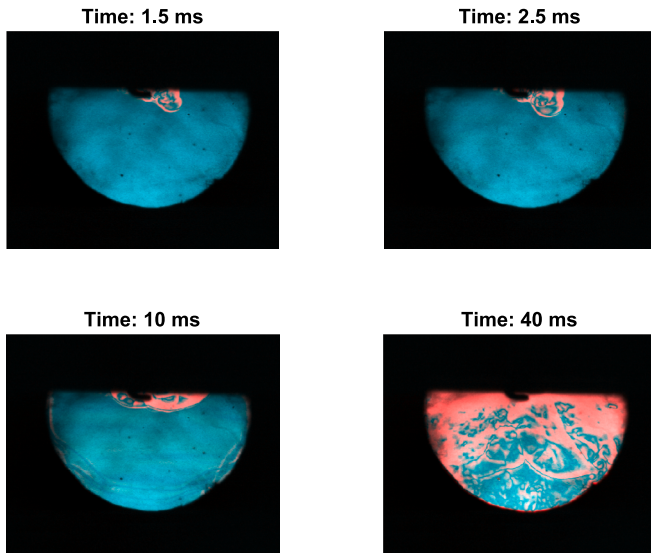
**Fig. 18.** Four frames of the high-speed Schlieren video for the lowest breakdown voltage where no HRR is detected (breakdown voltage of 6.6 kV,  $\lambda = 2.1$ ).

depicted for the two cases.

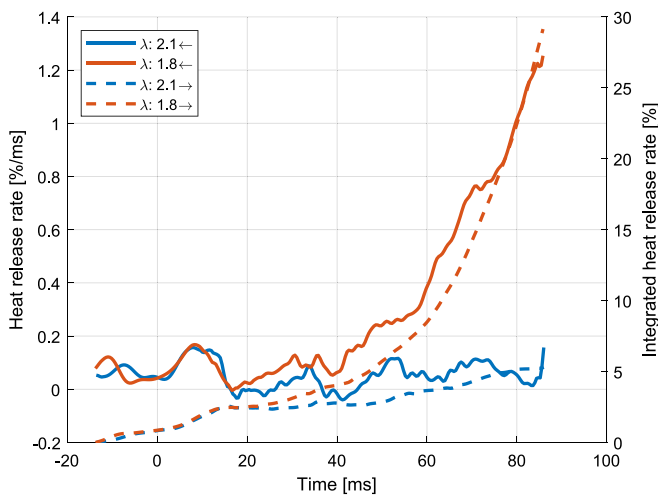
The breakdown voltage for the quenching experiment is four times higher than the one where the lowest breakdown voltage is recorded. The temperature during compression before combustion is approximately 500 K, while the burned temperatures exceed 2000 K for the depicted case. Similar pressures are present during compression stroke for the leaner case, while the burned temperature is lower and peaks at around 1650 K. The combustion process affects the pressure and the temperature in the unburned zone during the expansion stroke.

Fig. 16 shows the HRR analysis for five experiments in the RCEM. The colors are used to identify the different experiments with different  $\lambda$ . The solid line depicts the heat release rate, while the dashed line shows its integration (i.e., the cumulative heat released).

Lower  $\lambda$  gives, as expected, a faster heat release. For the experiments at  $\lambda$  values of 1.4, 1.5, and 1.6, the measurement window was long enough to capture the complete combustion event. For  $\lambda = 1.8$ , only a portion of the combustion process is captured. In contrast, ignition was not possible for  $\lambda = 2.1$ , or the inflammation phase took so long that capturing the HRR during the first 100 ms was not possible.



**Fig. 19.** Four frames of the high-speed Schlieren video for the highest breakdown voltage where the HRR is detected (breakdown voltage of 8.5 kV,  $\lambda = 1.8$ ).



**Fig. 20.** HRR of the two thresholds (quenching and ignition).

Fig. 17 shows the measured breakdown voltage of the control pulse against the ignition delay time ( $\Delta t_{\text{ign}}$ ), defined as the time between ignition and 10 % of mass fuel converted. Ten percent is used to avoid capturing very slow burning occurrences. All the experiments that could not reach 10 % fuel conversion are depicted on the furthest right of Fig. 17 and labeled “Quenching”.

The graph is divided into three regions. The red line is the one where all the breakdown voltage values are higher than the highest one where ignition was detected ( $>8.5$  kV). We call this the quenching voltage threshold. The green region is the region where all the recorded breakdown voltages lie below the lowest voltage recorded where no HRR was present (6.6 kV). This line is referred to as the ignition voltage threshold. The yellow area lies between these two thresholds (6.6–8.5 kV).

When faster burning cycles are present ( $<38$  ms), a breakdown voltage below the ignition voltage threshold is always measured. This means that these cycles can be divided from those where the flame quenches without superposition. The area between the two thresholds (yellow) outlines an area where combustion and quenching are hard to detect.

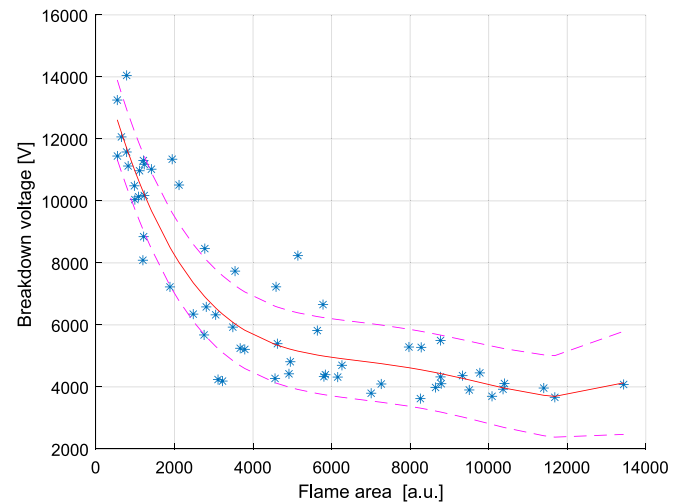


**Fig. 21.** Apparent flame area measured at 5 ms after ignition vs. breakdown voltage.

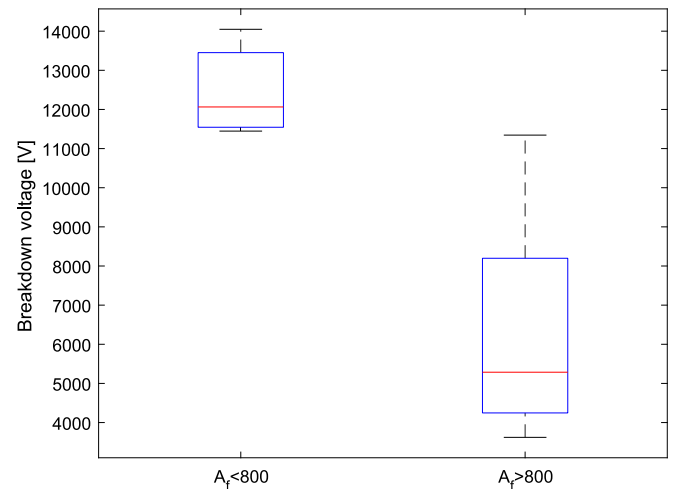


**Fig. 22.** Breakdown voltage of the control pulse vs. apparent flame area at 5 ms after ignition.

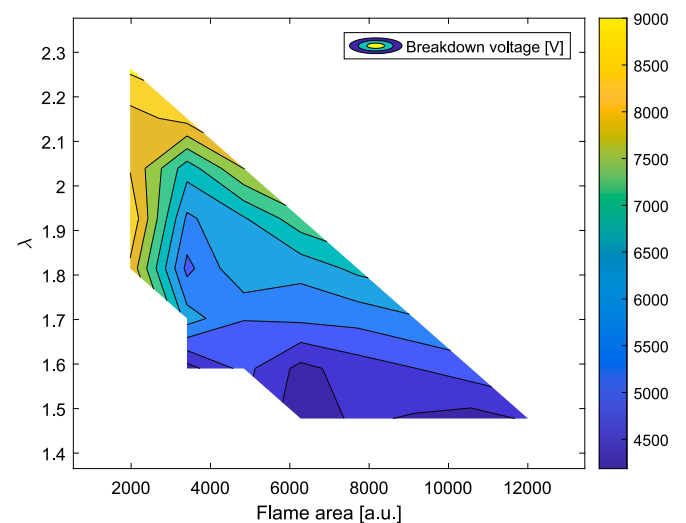


**Fig. 23.** Breakdown voltage variation as a function of apparent flame area and  $\lambda$ .



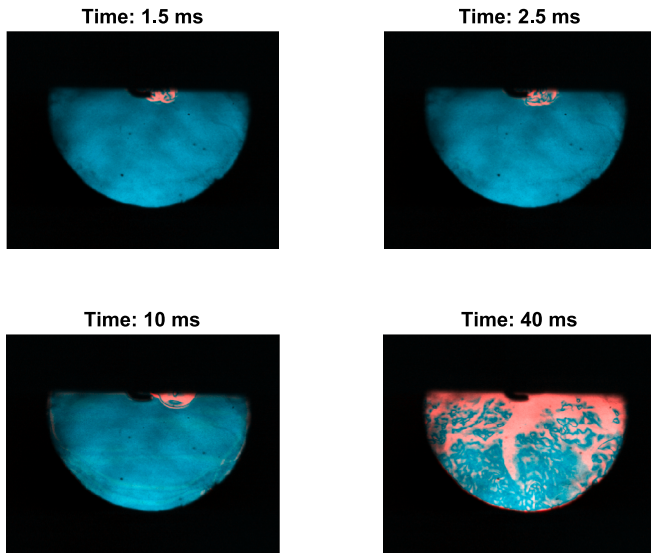


Fig. 24. Four frames of the high-speed Schlieren video where no HRR is detected (breakdown voltage of 8.1 kV,  $\lambda = 2$ ).

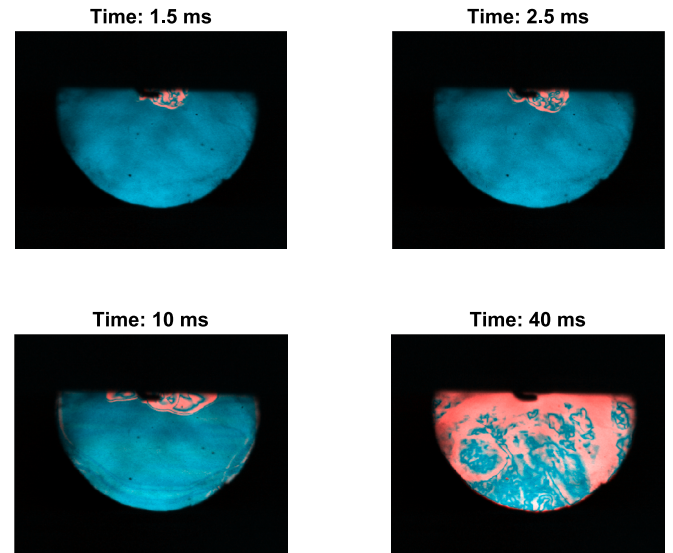


Fig. 26. Four frames of the high-speed Schlieren video where no HRR is detected (breakdown voltage of 6.6 kV,  $\lambda = 2.1$ ).

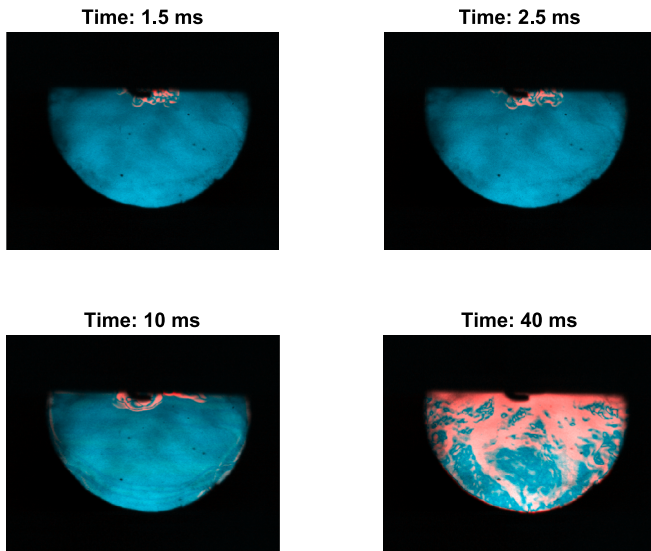


Fig. 25. Four frames of the high-speed Schlieren video where no HRR is detected (breakdown voltage of 7.2 kV,  $\lambda = 2.1$ ).

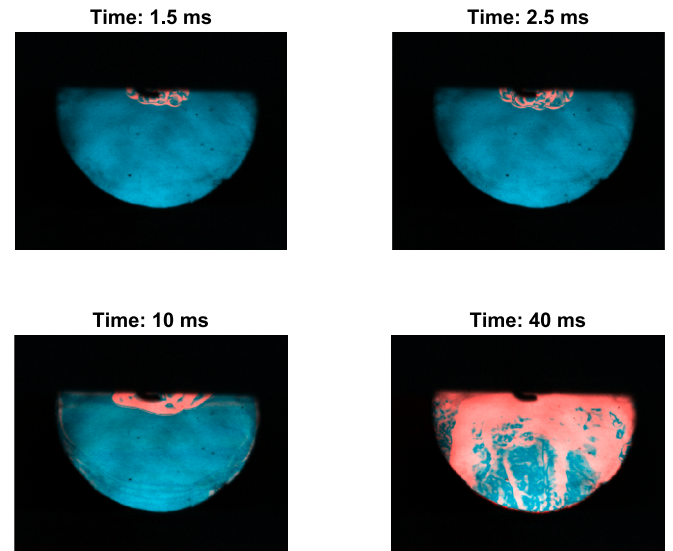


Fig. 27. Four frames of the high-speed Schlieren video where the HRR is detected (breakdown voltage of 7.7 kV,  $\lambda = 1.8$ ).

Fig. 18 depicts four frames of the Schlieren videos at 1.5, 2.5, 10, and 40 ms after the start of ignition for the point that defines the ignition voltage threshold line. The first frame shows the instant where the control pulse is applied.

Despite the very high overall  $\lambda$  of 2.1, a flame kernel is clearly visible which expands over the entire visible area.

Fig. 19 shows four Schlieren video frames (1.5, 2.5, 10, and 40 ms) for the point that defines the quenching voltage threshold.

The overall  $\lambda$  is 1.8, but similar images to the case of the ignition voltage threshold are present. Similar recordings are also visible for the other 6 cases in the yellow zone, two with no ignition and four with slow HRR. All the pictures of the flame propagation in this region are reported in Section 3.3.

Fig. 20 shows the HRR analysis for the points that define the two thresholds.

The same HRR is measured between the two experiments until 20 ms after ignition. After 20 ms for the experiment with the higher  $\lambda$  exponential growth versus time is present, while for the lower  $\lambda$  a slow linear

growth is found.

Fig. 21 shows the apparent flame area at 5 ms against the measured breakdown voltage of the control pulse. The apparent flame area is calculated with an arbitrary unit calculated as the number of all the pixels that are treated as flame (a.u.), as explained in Section 2.5. The red line represents a fit line between the data points, while the dashed pink lines represent the error (one- $\sigma$ ) around the fit.

The breakdown voltage of the control pulse decreases as the apparent flame area increases.

Fig. 22 groups all the experiments in two boxplots. On the left, the experiments with an apparent flame area at 5 ms below 800 a.u. ( $A_f < 800$ ) are shown, while on the right, those above 800 a.u. ( $A_f > 800$ ) are displayed.

The 800 a.u. apparent flame area at 5 ms divides the two breakdown groups without superposition, where lower breakdown voltages are present for larger apparent flame areas. The two groups present some overlap if later times or larger threshold flames are chosen.

Fig. 23 shows the breakdown voltage of the control pulse as a

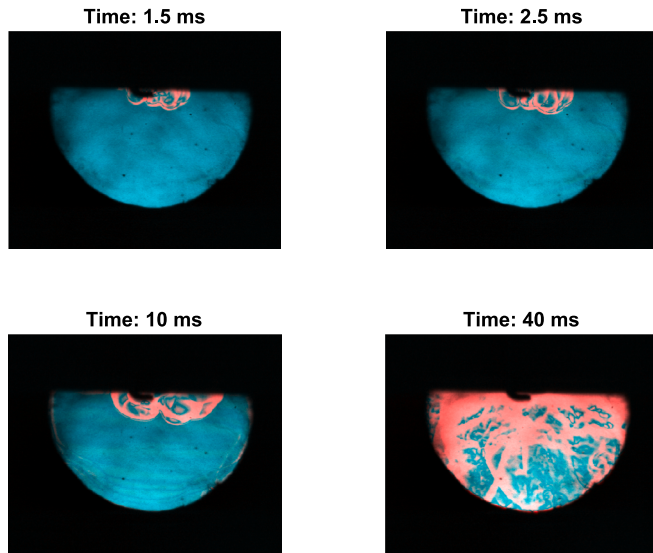


Fig. 28. Four frames of the high-speed Schlieren video where the HRR is detected (breakdown voltage of 7.2 kV,  $\lambda = 1.8$ ).

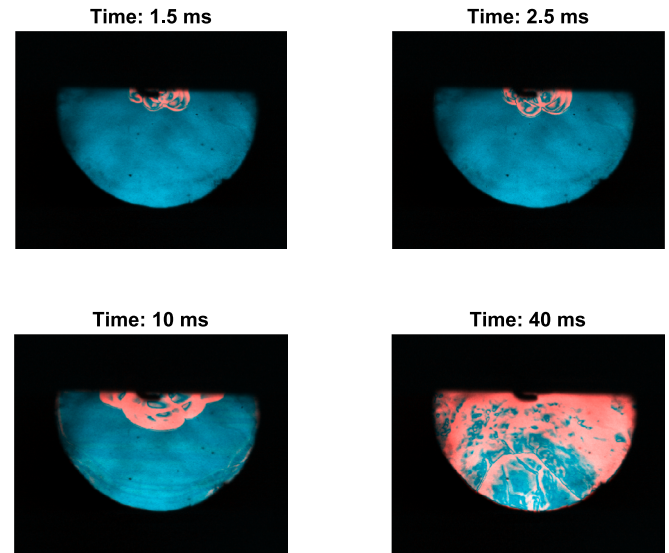


Fig. 30. Four frames of the high-speed Schlieren video where the HRR is detected (breakdown voltage of 8.2 kV,  $\lambda = 1.6$ ).

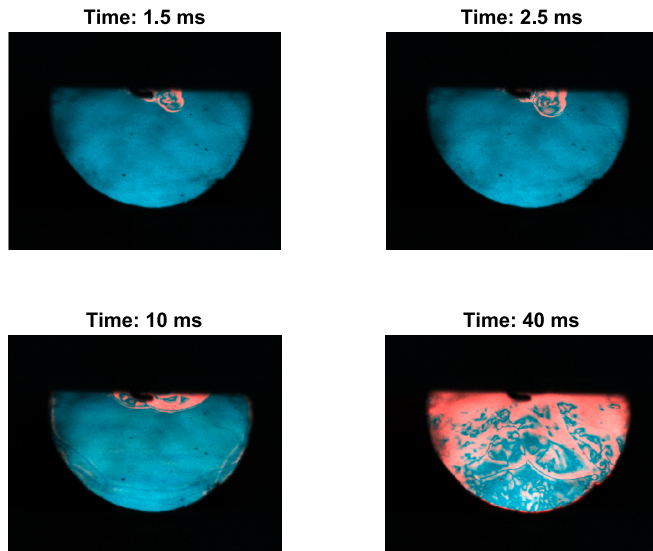


Fig. 29. Four frames of the high-speed Schlieren video where the HRR is detected breakdown voltage of 8.5 kV,  $\lambda = 1.8$ .

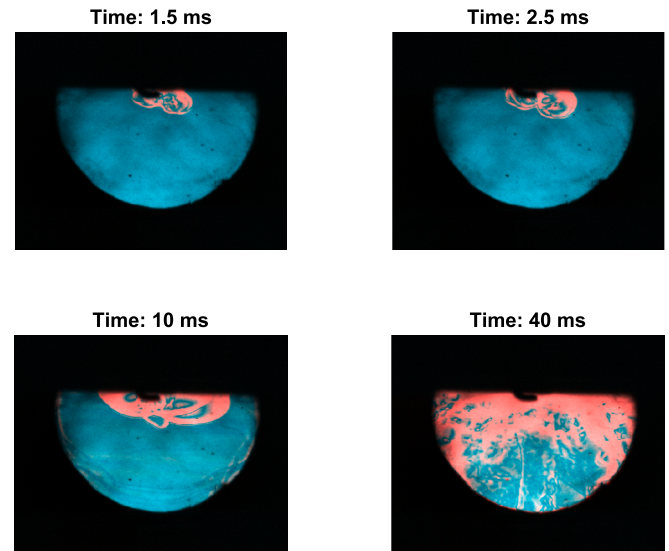


Fig. 31. Four frames of the high-speed Schlieren video where the HRR is detected (breakdown voltage of 6.7 kV,  $\lambda = 1.7$ ).

function of the flame area at 5 ms and the overall  $\lambda$ .

Lower breakdown voltages of the control pulse are present when larger initial flame kernels and lower AFR are present.

#### 4. Discussion

The discharge variation analysis shows that when a train of pulses at 10 kHz is applied, the breakdown voltage for subsequent pulses decreases. After a nanosecond discharge, the temperature between the electrodes is expected to be several tens of thousands of Kelvin [36]. Afterward, the plasma expansion and heat losses cool the region between the electrodes. After 100  $\mu$ s, the local density of the gas is still expected to be highly reduced; furthermore, ionized atoms and molecules can still be present between the electrodes, reducing the breakdown strength of the gas between the electrodes. A much higher breakdown voltage is present for the following pulses for the surface gap sparkplug. The reason is twofold. First, the geometry of the surface gap sparkplug results in a more homogeneous electric field, which can result

in a larger plasma surface; therefore, the energy is deposited over a broader volume. Second, the surface gap sparkplug has a higher heat range (NGK 7 vs. 12). The surface gap sparkplug has a better heat dissipation capability between the gap and the sparkplug thread. Both influences would result in a higher local density between the electrodes for the surface gap sparkplug, increasing its breakdown strength for subsequent pulses. The larger plasma surface could also explain the voltage decrease behavior during the pulse for the surface sparkplug, where slower decrease rates are measured. The energy during the pulse is deposited over a larger volume, reducing the temperature increase and, therefore, the ionization frequency and current growth. Different stray parameters are present due to the different geometries and construction of the sparkplugs under analysis. A higher stray inductance or lower stray capacitance of the surface sparkplug could also explain the slower voltage decrease rate after the breakdown.

The initial plasma kernel growth (up to ca. 100  $\mu$ s) is not affected by the AFR. Non-thermal plasma discharge simulations show a similar temperature profile for times below 100  $\mu$ s for different fuels and



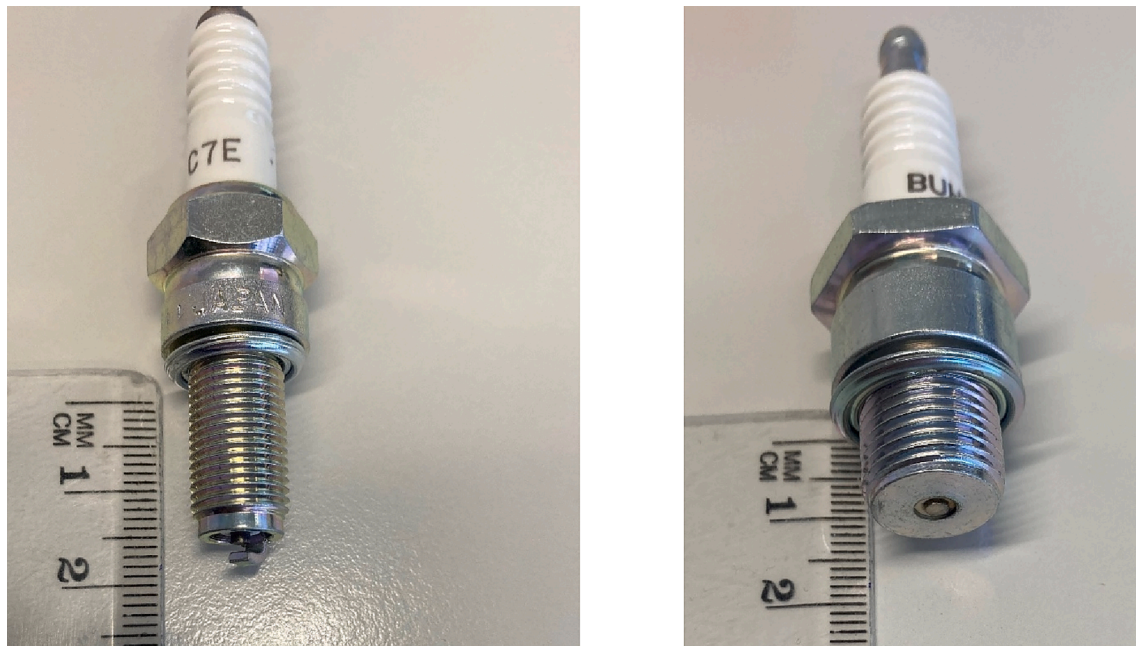


Fig. 32. J gap sparkplug (left), surface gap sparkplug (right).

dilutions [24]. After ca. 100  $\mu$ s, the early flame kernel is influenced by the in-cylinder conditions. During this phase, the kernel's presence, and dimension affect the local temperature and therefore the density. The breakdown strength of the gas is consequently also affected. The breakdown voltage of an additional pulse (control pulse) placed in this phase returns lower values when a strong kernel is present.

The possibility of using the control pulse breakdown voltage for ignition detection purposes is investigated at the ignitability limit inside the CVC. A lower breakdown voltage is observed when the ignition is successful. The ideal time for ignition detection is different for the two investigated sparkplugs, probably depending on the sparkplug's heat range, the number of pulses used in the main ignition sequence, and the different gas densities and compositions. There is an ideal dwell time for the delay between the end of the main ignition sequence and the control pulse between 0.5 and 5 ms. When the dwell time is too short, the breakdown voltage value is still affected by the previous discharge, while when the delay is too long, the local density between the electrodes decreases back to the value typical of quenching conditions.

The breakdown voltage for ignition and quenching experiments in the CVC shows some overlap. One reason is that the breakdown voltage value under nanosecond pulses naturally scatters due to the stochastic nature of the seed electron appearance. Furthermore, even if an early flame could be formed and correctly detected by the ignition detection technique, the flame could quench at a later stage without giving a measurable pressure rise. Conversely, when the control pulse detects no early flame, this pulse could be the one responsible for starting the combustion process. From the analysis in the RCEM, these extreme cases can be recognized thanks to Schlieren imaging and a detailed heat release analysis.

Inside the RCEM, experiments at different  $\lambda$  are performed. The dwell time between the last pulse of the main ignition sequence and the control pulse is 1 ms for all experiments. This time delay is insufficient in all the experiments for an appreciable pressure increase due to combustion. The only factors that can explain a decrease in gas breakdown strength are higher local temperature (density) and/or higher density of active and excited species, both reducible to the presence of a flame kernel.

The breakdown voltage of the control pulse increases with increasing  $\lambda$ . This is in line with the theory behind the ignition detection method. The heat losses between the burned gas present between the electrodes and the flame kernel are lower if  $\lambda$  is lower due to the higher

flame temperatures. Similar effects are reported in [18], where higher voltage strengths are present in the flame front of reacting mixtures for higher AFRs. The minimum voltage necessary to have a breakdown when the flame arrived at the sparkplug increased from 3.3 kV to 4 kV for a  $\lambda$  increase from 1.2 to 1.6 [18]. The voltage increase ratio is inversely proportional to the adiabatic flame temperature ratio (2080 K vs. 1730 K).

The authors attribute the higher breakdown strength to the lower ion density and temperatures present in the flame front of diluted combustion, having lower reaction rates.

From the heat release rate analysis, it is clear that the fast-burning cycles and the cycles where no initial flame kernel is visible are distinguishable from their breakdown voltage value. The cycles with ignition delay times below 38 ms have a breakdown voltage lower than 6 kV, which is less than the lowest recorded breakdown voltage of 6.6 kV present when no HRR is present.

Experiments with lower HRR sometimes overlap with experiments where no HRR is detected. Similar flame kernels are detected from the Schlieren video analysis for these experiments. The difference in HRR rises in a later stage of combustion, as is visible from the HRR analysis.

The breakdown voltage's control pulse decreases with lower AFRs and larger areas of the initial flame kernels. Both effects result in lower local density between the electrodes. On the one hand, lower  $\lambda$  results in higher local temperatures and, therefore, lower density. On the other hand, a larger flame area reduces the surface-to-volume ratio reducing the specific heat losses. This influence further explains the overlapping experiments where similar local density (i.e., breakdown voltage) can be found in experiments with a large flame area and a high  $\lambda$  or experiments having a small flame area and a lower  $\lambda$  value.

The prospective voltage of the control pulse remains constant for all the experiments, and the breakdown voltage for all the experiments in the RCEM occurs during the rising part of the nanosecond pulse (Fig. 15). Therefore as investigated in [21,22], the breakdown voltage linearly depends on the gas density. The highest measured breakdown voltage in the RCEM is approximately four times higher than the lowest. This correlates well with the temperature ratio of the burned gas ( $\sim 2000$  K) estimated with the two-zone thermodynamic analysis calculated for the experiments with a fast HRR and temperatures before combustion of 500 K, which is the temperature present in the RCEM at ignition timing due to the polytropic compression. Since the difference



between the unburned and burned zone decreases for increasing AFR, the maximal possible density ratio decreases. Nevertheless, with a compression temperature of 900 K (typical of engines) and a highly diluted combustion ( $\lambda = 2$ ) the adiabatic flame temperature is above 1900 K, which still gives theoretical density ratios between unburned and burned zone above 2.

## 5. Conclusions

The presented ignition detection technique provides the possibility of combustion monitoring based on the breakdown voltage value of an additional pulse during inflammation after ignition. Several factors influence the breakdown voltage value: the sparkplug geometry and its heat range, the initial pressure, and temperature, the rising rate of the applied voltage, the number of pulses of the main ignition sequence, etc. Nevertheless, if most factors are kept constant, the technique is a reliable ignition diagnostic technique. A further limitation of the proposed method is the ideal location of the control pulse. The sooner the failed ignition is detected, the more time is available to react to quenching. The disadvantage of short dwell times is that later flame quenching is impossible to capture, as has been seen in some RCEM experiments with a high air excess ratio.

This technique offers the advantage of being a very fast detection method. The breakdown voltage value is affected by the inflammation process only a few hundred microseconds after the ignition event, well before there is an increase in pressure due to the heat release. The control pulse is applied in the CVC before the pressure increases and in the RCEM before the pressure deviates from polytropic compression. Such a velocity of detection is usually reserved for optical detection methods. Nevertheless, the proposed technique only relies on measuring the breakdown voltage of one additional discharge after ignition in the same location. This gives the theoretical possibility of fast closed-loop control of ignition with NRPD, where additional pulses are delivered to better ignite the mixtures when a high breakdown voltage of the control pulse is present. Even a coupling of fast ignition detection with a direct fuel injection system could be possible, allowing the possibility of providing more fuel before a new ignition attempt.

For in-vehicle applications, one approach for monitoring the success of ignition is the shunt measurement in the middle of the high-voltage cable, which gives the advantage of no need to place a voltage probe near the sparkplug. Furthermore, if the supplied pulse is stable throughout the operations, ignition success can be characterized only by the reflected voltage's maximal value. Since a typical engine ECU does not have a sufficient sampling rate to represent the shunt measurement, a trigger circuit could be applied, for example, to stop the ignition process when the reflected voltage falls below a given threshold.

Since the breakdown voltage of the control pulse decreases with decreasing  $\lambda$ , the technique could also be used to detect  $\lambda$  at the sparkplug location in applications where this measurement is impossible, for example, in active pre-chambers and stratified combustion. The precision of the technique is limited, but a deviation in  $\lambda$  of ca. 0.2 is feasible to detect with one-sigma confidence in the RCEM (Fig. 12). If the  $\lambda$  estimation goal is the optimization of variables such as injection timing or duration inside an active pre-chamber, the repetition of the measurement could increase the precision of the estimation.

Because multi-spark inductive coils are currently state-of-the-art ignition systems in various vehicles, this technique could probably also be applied without an NRPD ignition system. Nevertheless, one problem is counterintuitively bounded by the fast-rising pulse nature of NRPD. One would assume that the breakdown voltage value scatter would decrease with decreasing voltage gradients. Nevertheless, the dependence of the seed electron generation rate on a reduced electric field could result in less scatter with NRPD, making this diagnostic technique not applicable or less precise with comparable slow-increasing voltage systems. Therefore, the ignition diagnostic technique in future works should also be investigated with state-of-the-art

multi-spark ignition systems.

The current investigation is performed in setups where the charge motion is nonexistent (CVC) or highly reduced (RCEM) when compared to internal combustion engines. Turbulence could move the flame kernel away from the electrodes making the detection more difficult. In future research, the effect of turbulence on the ignition diagnostic technique should be evaluated in SI-Engines. After assessment in engines, the technique could be applied, for example, to reduce cycle-to-cycle variability.

## CRediT authorship contribution statement

**M. Balmelli:** Conceptualization, Methodology, Software, Formal analysis, Investigation, Writing – original draft, Visualization. **L. Merotto:** Validation, Resources, Writing – review & editing. **P. Soltic:** Validation, Resources, Writing – review & editing, Supervision, Project administration, Funding acquisition. **J. Biela:** Validation, Writing – review & editing, Supervision.

## Declaration of Competing Interest

The authors declare that they have no known competing financial interests or personal relationships that could have appeared to influence the work reported in this paper.

## Data availability

Data will be made available on request.

## Acknowledgments

The authors thank Bruno Schneider for his valuable help in recommissioning the RCEM machine. The authors also thank Peter Obrecht for the valuable inputs for the heat release rate analysis.

## Appendix A

### A.1. Schlieren imaging

a.1 Schlieren images for the experiments without heat release rate but breakdown voltage below the quenching voltage threshold.

See Figs. 24–26.

a.2 Schlieren images for the experiments with heat release rate but breakdown voltage above the ignition voltage threshold.

See Figs. 27–31.

### A.2. Sparkplugs

Fig. 32 shows the two different sparkplugs used in the present work a J-gap sparkplug (NGK 5096) and a surface gap sparkplug (NGK 2522).

## Appendix B. Supplementary material

Supplementary data to this article can be found online at <https://doi.org/10.1016/j.enconman.2023.117382>.

## References

- [1] Hilliard JC, Springer GS, editors. Fuel economy. Boston, MA: Springer US; 1984. doi: 10.1007/978-1-4899-2277-9.
- [2] Cho HM, He B-Q. Spark ignition natural gas engines—a review. Energy Convers Manag 2007;48:608–18. <https://doi.org/10.1016/j.enconman.2006.05.023>.
- [3] Reitz RD, Ogawa H, Payri R, Fansler T, Kokjohn S, Moriyoshi Y, et al. IJER editorial: the future of the internal combustion engine. Int J Engine Res 2020;21: 3–10. <https://doi.org/10.1177/1468087419877990>.

- [4] Pancheshnyi SV, Lacoste DA, Bourdon A, Laux CO. Ignition of propane-air mixtures by a repetitively pulsed nanosecond discharge. *IEEE Trans Plasma Sci* 2006;34: 2478–87. <https://doi.org/10.1109/TPS.2006.876421>.
- [5] Zhai J, Lee S-Y, Zhao Z, Singleton D. Study of flame kernel development at high EGR and high flow speed using conventional spark igniter and non-thermal plasma under gasoline engine relevant conditions. *Combust Sci Technol* 2022;1–21. <https://doi.org/10.1080/00102202.2022.2138711>.
- [6] Starikovskaia SM. Plasma assisted ignition and combustion. *J Phys Appl Phys* 2006; 39:R265–99. <https://doi.org/10.1088/0022-3727/39/16/R01>.
- [7] Merotto L, Balmelli M, Vera-Tudela W, Soltic P. Comparison of ignition and early flame propagation in methane/air mixtures using nanosecond repetitively pulsed discharge and inductive ignition in a pre-chamber setup under engine relevant conditions. *Combust Flame* 2022;237:111851. <https://doi.org/10.1016/j.combustflame.2021.111851>.
- [8] Vera-Tudela W, Merotto L, Balmelli M, Soltic P. Experimental study of the ignition of lean methane/air mixtures using inductive and NRPD ignition systems in the pre-chamber and turbulent jet ignition in the main chamber. *Energy Convers Manag* 2021;115012. <https://doi.org/10.1016/j.enconman.2021.115012>.
- [9] Shiraishi T, Urushihara T, Gundersen M. A trial of ignition innovation of gasoline engine by nanosecond pulsed low temperature plasma ignition. *J Phys Appl Phys* 2009;42:135208. <https://doi.org/10.1088/0022-3727/42/13/135208>.
- [10] Tropina AA, Kuzmenko AP, Marasov SV, Vilchinsky DV. Ignition system based on the nanosecond pulsed discharge. *IEEE Trans Plasma Sci* 2014;42:3881–5. <https://doi.org/10.1109/TPS.2014.2339654>.
- [11] Cathey CD, Tang T, Shiraishi T, Urushihara T, Kuthi A, Gundersen MA. Nanosecond plasma ignition for improved performance of an internal combustion engine. *IEEE Trans Plasma Sci* 2007;35:1664–8. <https://doi.org/10.1109/TPS.2007.907901>.
- [12] Barbosa S, Pilla G, Lacoste DA, Scouffaire P, Ducruix S, Laux CO, et al. Influence of nanosecond repetitively pulsed discharges on the stability of a swirled propane/air burner representative of an aeronautical combustor. *Philos Trans R Soc Math Phys Eng Sci* 2015;373:20140335. <https://doi.org/10.1098/rsta.2014.0335>.
- [13] Malé Q, Shcherbanev S, Noiray N. Numerical study of plasma assisted combustion in a sequential combustor. S1540748922000190 *Proc Combust Inst* 2022. <https://doi.org/10.1016/j.proci.2022.06.016>.
- [14] Eriksson L, Nielsen L. Ionization current interpretation for ignition control in internal combustion engines. *Control Eng Pract* 1997;5:7.
- [15] Auzins J, Johansson H, Nytoft J. Ion-gap sense in misfire detection, knock and engine control; 1995. p. 950004. doi: 10.4271/950004.
- [16] Irimescu A, Merola SS, Maria Vaglieco B. Spark anemometry applied through secondary current measurements in an optical spark ignition engine. *Energy Convers Manag* 2022;269:116088. doi: 10.1016/j.enconman.2022.116088.
- [17] Kosmadakis GM, Rakopoulos DC, Arroyo J, Moreno F, Muñoz M, Rakopoulos CD. CFD-based method with an improved ignition model for estimating cyclic variability in a spark-ignition engine fueled with methane. *Energy Convers Manag* 2018;174:769–78. <https://doi.org/10.1016/j.enconman.2018.08.093>.
- [18] Wang L, Yu X, Cong B, Li L, Chen G, Zheng M. Active plasma probing for lean burn flame detection. *Detroit, Michigan, United States*; 2023. p. 2023-01-0293. doi: 10.4271/2023-01-0293.
- [19] Heywood JB. *Internal combustion engine fundamentals*. New York: McGraw-Hill; 1988.
- [20] Kammermann T, Giannakopoulos GK, Koch J, Soltic P, Boulouchos K. Early flame propagation of hydrogen enriched methane-air mixtures at quasi laminar conditions in a rapid compression expansion machine. *Int J Hydrog Energy* 2019; 44:27107–22. <https://doi.org/10.1016/j.ijhydene.2019.08.155>.
- [21] Balmelli M, Lu Y, Farber R, Merotto L, Soltic P, Bleiner D, et al. Breakdown of synthetic air under nanosecond pulsed voltages in quasi-uniform electric fields. *IEEE Access* 2022;10:53454–67. <https://doi.org/10.1109/ACCESS.2022.3175460>.
- [22] Balmelli M, Farber R, Merotto L, Soltic P, Bleiner D, Franck CM, et al. Experimental analysis of breakdown with nanosecond pulses for spark-ignition engines. *IEEE Access* 2021;9:100050–62. <https://doi.org/10.1109/ACCESS.2021.3095664>.
- [23] Shcherbanev SA, Malé Q, Dharmaputra B, Solana-Pérez R, Noiray N. Effect of plasma-flow coupling on the ignition enhancement with non-equilibrium plasma in a sequential combustor. *J Phys Appl Phys* 2022;55:425202. <https://doi.org/10.1088/1361-6463/ac82fa>.
- [24] Gururajan V, Scarcelli R, Biswas S, Ekoto I. CFD modeling of low temperature ignition processes from a nanosecond pulsed discharge at quiescent conditions. In: ICEF2021, ASME 2021 internal combustion engine division fall technical conference; 2021. doi: 10.1115/ICEF2021-67902.
- [25] Kammermann T, Merotto L, Bleiner D, Soltic P. Spark-induced breakdown spectroscopy for fuel-air equivalence ratio measurements at internal combustion engine-relevant conditions. *Spectrochim Acta Part B: At Spectrosc* 2019;155: 79–89. <https://doi.org/10.1016/j.sab.2019.03.006>.
- [26] Kammermann T, Kreutner W, Trottmann M, Merotto L, Soltic P, Bleiner D. Spark-induced breakdown spectroscopy of methane/air and hydrogen-enriched methane/air mixtures at engine relevant conditions. *Spectrochim Acta Part B: At Spectrosc* 2018;148:152–64. <https://doi.org/10.1016/j.sab.2018.06.013>.
- [27] Gerke U. Numerical analysis of mixture formation and combustion in a hydrogen direct-injection internal combustion engine. *ETH Zurich*; 2007. doi: 10.3929/ETHZ-A-005540349.
- [28] Schlatter S, Schneider B, Wright YM, Boulouchos K. Comparative study of ignition systems for lean burn gas engines in an optically accessible rapid compression expansion machine; 2013. p. 2013-24-0112. doi: 10.4271/2013-24-0112.
- [29] Schlatter S, Schneider B, Wright Y, Boulouchos K. Experimental study of ignition and combustion characteristics of a diesel pilot spray in a lean premixed methane/air charge using a rapid compression expansion machine; 2012. p. 2012-01-0825. doi: 10.4271/2012-01-0825.
- [30] Mitakos DA. Experimental investigations for phenomenological modelling of two-stage auto-ignition under HCCI conditions. *ETH Zurich*; 2014. doi: 10.3929/ETHZ-A-010421729.
- [31] Ramo S, Van Duzer T, Whinnery JR. *Fields and waves in communication electronics*. 3rd ed. New York: Wiley; 1994.
- [32] Küchler A. *High voltage engineering*. Berlin, Heidelberg: Springer Berlin Heidelberg; 2018. doi: 10.1007/978-3-642-11993-4.
- [33] Tholin F, Bourdon A. Influence of the external electrical circuit on the regimes of a nanosecond repetitively pulsed discharge in air at atmospheric pressure. *Plasma Phys Control Fusion* 2015;57:014016. <https://doi.org/10.1088/0741-3335/57/1/014016>.
- [34] Obrecht P. WEG, Rechenprogramm zur Berechnung des Wärmeentwicklungs-gesetzes aus gemessenen Brennraumdruckverläufen von Diesel- und Ottomotoren, Benutzerhandbuch und Programmdokumentation. Zürich: ETHZ IET-LAV; 2005.
- [35] Minesi N, Stepanyan S, Mariotto P, Stancu GD, Laux CO. Fully ionized nanosecond discharges in air: the thermal spark. *Plasma Sources Sci Technol* 2020;29:085003. <https://doi.org/10.1088/1361-6595/ab94d3>.
- [36] Minesi N. Thermal spark formation and plasma-assisted combustion by nanosecond repetitive discharges n.d.;304.